SCIENTIFIC REP⚙RTS

OPEN

Highly Efficient Perovskite Solar Cells with Substantial Reduction of Lead Content

Chong Liu[1], Jiandong Fan[1,2], Hongliang Li[1], Cuiling Zhang[1] & Yaohua Mai[1,2]

Despite organometal halide perovskite solar cells have recently exhibited a significant leap in efficiency, the Sn-based perovskite solar cells still suffer from low efficiency. Here, a series homogeneous $CH_3NH_3Pb_{(1-x)}Sn_xI_3$ ($0 \leq x \leq 1$) perovskite thin films with full coverage were obtained via solvent engineering. In particular, the intermediate complexes of $PbI_2/(SnI_2)\cdot(DMSO)_x$ were proved to retard the crystallization of $CH_3NH_3SnI_3$, thus allowing the realization of high quality Sn-introduced perovskite thin films. The external quantum efficiency (EQE) of as-prepared solar cells were demonstrated to extend a broad absorption minimum over 50% in the wavelength range from 350 to 950 nm accompanied by a noteworthy absorption onset up to 1050 nm. The $CH_3NH_3Pb_{0.75}Sn_{0.25}I_3$ perovskite solar cells with inverted structure were consequently realized with maximum power conversion efficiency (PCE) of 14.12%.

Perovskite solar cells have transfixed researchers in the solar energy field since its power conversion efficiency (PCE) was increased up to 22.1% in only 6 years, which outperformed other photovoltaic technologies[1–7]. Although soaring efficiencies enable this technology to be potentially commercialized, there remains skepticism concerning its intrinsic toxicity and instability[8–10]. The lead element presented in perovskite solar cells could possibly leach out of the solar panel onto the rooftops or the soil below, even though the cells are encapsulated.

Increasingly broad types of lead-free compositions are being investigated to obtain new ones as the alternative elements, e.g. Sn, Ge, Cu etc. Amongst, the Sn was demonstrated to be capable of replacing/partly substituting for lead in perovskite solar cells[11–13], although the organic Sn-based compounds were demonstrated to pass easily from the respiratory system to the bloodstream due to their solubility in fat[14,15]. Methylammonium tin halide perovskites ($CH_3NH_3SnI_{3-x}Br_x$) have been used as lead-free light harvesters for solar cell applications for the first time by Mercouri G. Kanatzidis *et al.*, which enabled the realization of lead-free solar cells and lead to a promising initial PCE of 5.73%[16]. Meanwhile, they demonstrated that alloyed perovskite solid solutions of methylammonium tin iodide and its lead analogue ($CH_3NH_3Pb_{1-x}Sn_xI_3$) are implemented as novel panchromatic light absorbing material in solar cell, which allowed extending the absorbance to 1050 nm[11]. Almost the same time, Henry Snaith and co-authors presented the $CH_3NH_3SnI_3$ perovskite solar cell that processed on a mesoporous TiO_2 scaffold, reaching efficiencies of over 6%[17]. Later on, Feng Hao *et al.* reported a solvent-mediated crystallization process to obtain a pinhole-free, highly uniform $CH_3NH_3SnI_3$ thin film, in which the dimethyl sulfoxide (DMSO) solution was employed to form the transitional $SnI_2\cdot3DMSO$ intermediate phase[18]. Very recently, Seok *et al.* used the homogeneous dispersion of SnF_2 through the formation of the SnF_2-pyrazine complex to fabricate formamidinium tin iodide ($FASnI_3$) PSCs with PCE of 4.8%[19]. Despite the fabrication was carried out in the nitrogen atmosphere in a glove box, the Sn^{2+} was easily oxidized into Sn^{4+} due to its instability. Therefore, the highest PCE of completely lead-free perovskite solar cells was only 6%, even for the Sn-involved perovskite solar cell, its maximum PCE still remained around 7%, which was not comparable to the lead-based perovskite solar cells that rose up to 22.1% recently. In this scenario, it is enlightening to realize competitive photovoltaic properties using lead-free organic–inorganic compounds toward commercial applications of perovskite solar cells.

In this communication, we used DMSO as the solvent mediation to form the $PbI_2/(SnI_2)\cdot(DMSO)_x$ complexes, which gave rise to the formation of satisfied $CH_3NH_3Pb_{(1-x)}Sn_xI_3$ ($0 \leq x \leq 1$) thin films. The tunable bandgap by different x values allowed realizing an efficient Sn-based inverted perovskite solar cell with a maximum PCE of 14.12%.

[1]Institute of Photovoltaics, College of Physics Science and Technology, Hebei University, Baoding, 071002, China. [2]Institute of New Energy Technology, College of Information and Technology, Jinan University, Guangzhou, 510632, China. Correspondence and requests for materials should be addressed to J.F. (email: jdfan@jnu.edu.cn) or Y.M. (email: yaohuamai@jnu.edu.cn)
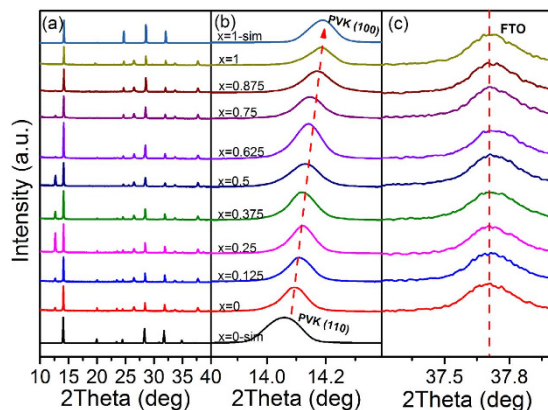
Figure 1. (**a**) XRD patterns of as-prepared $CH_3NH_3Pb_{(1-x)}Sn_xI_3$ ($0 \leq x \leq 1$) thin films with different Sn concentrations; (**b**) The detailed transition of the peak varied from (110) to (100) with different Sn concentrations; (**c**) The corresponding FTO peaks.

Results

Preparations and characterizations of $CH_3NH_3Pb_{(1-x)}Sn_xI_3$ ($0 \leq x \leq 1$) perovskite thin films.

Herein, the $CH_3NH_3Pb_{(1-x)}Sn_xI_3$ ($0 \leq x \leq 1$) perovskite thin films were prepared by a two-step solution-processed technique that was able to control the crystallization rate of $CH_3NH_3SnI_3$, which solved the problem of uncontrollable crystal growth due to its habitual nature of easier crystallization even at room temperature[17]. In our previous study, we employed DMSO to complex PbI_2 in the case of pure $CH_3NH_3PbI_3$[20], by which, the obtained $PbI_2 \cdot (DMSO)_x$ ($0 \leq x \leq 1.86$) complexes were proved to be capable of retarding the crystallization of PbI_2. Here, the DMSO was used to complex the PbI_2 and SnI_2 separately via solvent engineering. We carefully studied the influence of precursor concentration of $PbI_2 \cdot (DMSO)_x$ and $SnI_2 \cdot (DMSO)_x$ on the thin films and the corresponding solar cells. The Sn precursor solution varied from 0 to $80 \, \mu L$ with a total volume ($80 \, \mu L$) of Sn and Pb as mentioned in the experimental section. The corresponding values of x in $CH_3NH_3Pb_{(1-x)}Sn_xI_3$ were in the range from 0 to 1. It should be noted that the insitu complex thin films were amorphous and the corresponding XRD peaks were not able to be detected prior to post-annealing treatment. As shown in Supplementary Fig. 1 and Supplementary Fig. 2a, in the case of $x = 0$, the $PbI_2 \cdot (DMSO)_x$ complex was formed as expected, which was consistent with our previous report[20]. While the Sn was introduced, the peaks that assigned to be $SnI_2 \cdot (DMSO)_x$ complex were also observed (Supplementary Fig. 1). To further clarify the presence of the intermediates, we carried out the FTIR characterizations of the as-prepared intermediate layers (Supplementary Fig. 2), which were deposited from DMSO/dimethylformamide (DMF) solution before and after annealing. The FTIR spectra show the characteristic C−S and C−O stretching vibrations from the Sn^{2+}- and/or Pb^{2+}- coordinated DMSO solvent at 960 and $1012 \, cm^{-1}$, and C=O stretching vibrations from the Sn^{2+}- and/or Pb^{2+}- coordinated DMF solvent at 1389 and $1688 \, cm^{-1}$. After heated at 60 °C for 10 min, the stretching vibrations of C=O were disappeared while the C−S and C−O stretching vibrations were still exist. Combined with the XRD results (Supplementary Fig. 1), we can come to a conclusion that $SnI_2(DMSO)_x$ and/or $PbI_2(DMSO)_x$ were formed at relatively low temperatures, respectively[18]. Upon annealing at 140 °C, we found that the characteristic modes of the DMSO molecule disappeared, thus confirming the complete removal of the intermediate compound. Additionally, we found that the grain size of Sn-based complex had a significant enhancement in comparison to the one of PbI_2-based complex, which was associated with the properties of easy crystallization and fast growth rate for SnI_2 (Supplementary Fig. 3a,b). We assumed that the SnI_2 dominated the complexed process in the copresence of SnI_2 and PbI_2 that dissolved in DMSO and DMF precursor solution. There was no any complex detected once the solvent without DMSO in the case $x = 1$ (Supplementary Fig. 1 and Fig. 3d). The highly crystallized SnI_2 single crystal film with lower coverage prohibited the further process to fabricate solar cells.

As expected, the copresence of $PbI_2 \cdot (DMSO)_x$ and $SnI_2 \cdot (DMSO)_x$ complexes were demonstrated to slow down the crystallization of $CH_3NH_3Pb_{(1-x)}Sn_xI_3$ ($0 \leq x \leq 1$) perovskite thin films. Figure 1 displays the XRD evolution of prepared $CH_3NH_3Pb_{(1-x)}Sn_xI_3$ ($0 \leq x \leq 1$) thin films while the involved volume of Sn precursor solution varied from $x = 0$ to $x = 1$. Prior to XRD characterizations, we simulated the XRD patterns of $x = 0$ and $x = 1$, which represented the $CH_3NH_3PbI_3$ and $CH_3NH_3SnI_3$, respectively. The simulated results revealed that the perovskite phase altered from tetragonal phase ($x = 0$, $CH_3NH_3PbI_3$, P4 mm (α-phase)) to cubic phase ($x = 1$, $CH_3NH_3SnI_3$, I4 cm (β-phase)). As shown in Fig. 1, the (110) peak of perovskite gradually moved from 14.1° to 14.2° corresponding to (100) plane in cubic phase while the Sn introduction amount improved from $x = 0$ to $x = 1$, whereas the FTO peaks remained stable. Additionally, the two peaks located at 23.5° and 24.5° were respectively assigned to be (211) and (202) in the case of $CH_3NH_3PbI_3$. With the x value increasing, these two peaks tent to merge to be a single peak corresponding to the (113) plane in the P4 mm space group ($CH_3NH_3SnI_3$). Such evolution suggested a distortion of the relative positions of the octahedra along the 4-fold crystallographic axis. It turns out that the involved Sn induced the alteration of the perovskite phase, which is consistent with the previous report[11].

Meanwhile, the superfluous PbI_2/SnI_2 appeared when the Sn involved inside the perovskite thin films as shown in Fig. 1a. It can also be certified by the morphology of perovskite thin film as shown in SEM images
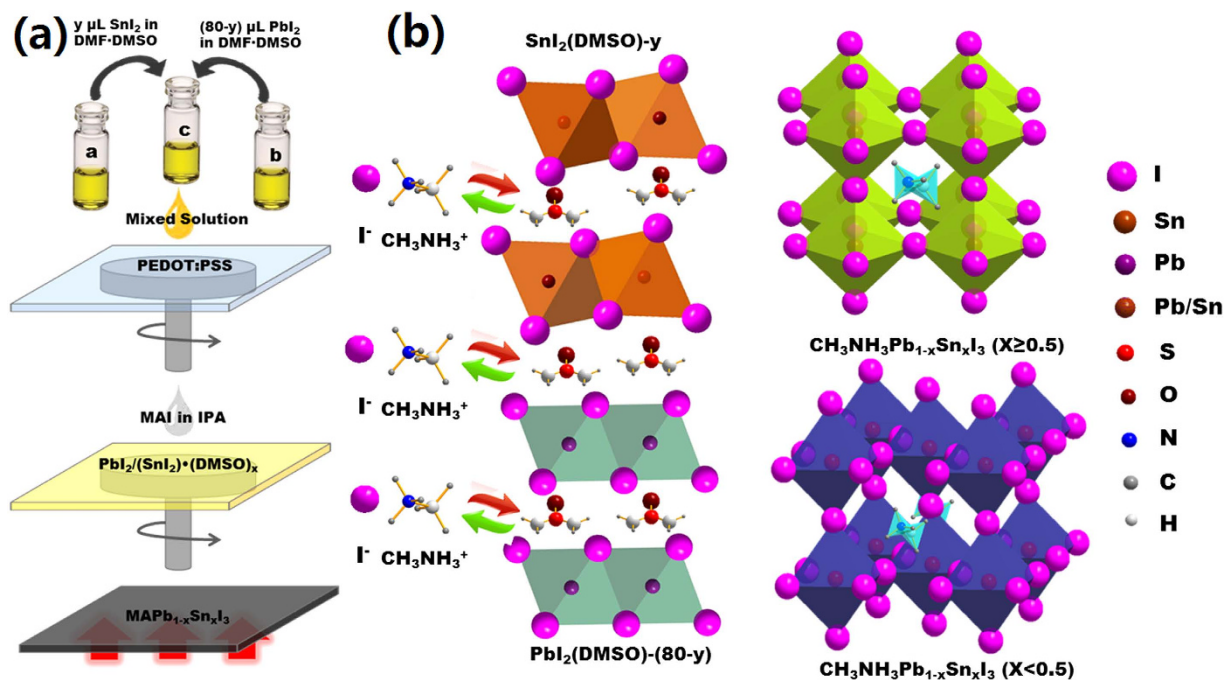
Figure 2. (**a**) Schematic of prepared process of $CH_3NH_3Pb_{(1−x)}Sn_xI_3$ ($0 \leq x \leq 1$) thin films; (**b**) Schematic of formation mechanism in $CH_3NH_3Pb_{(1−x)}Sn_xI_3$ ($0 \leq x \leq 1$) thin films and the corresponding crystal structure.

(Supplementary Fig. 4). As previously reported[21–23], the sporadic formation of PbI_2/SnI_2 species in the grain boundaries might give rise to a successful passivation that forms energy barriers to prevent excitons from the surface defects and/or traps states.

We then proposed the potential mechanism in the kinetic process of perovskite crystal growth in the presence of DMSO as shown in Fig. 2. Here, the PbI_2/SnI_2 can be intercalated by DMSO solvent mediation, which gives rise to the formation of $PbI_2/(SnI_2)\cdot(DMSO)_x$ complexes (Fig. 2a). During the complexing process, the DMSO solvent is advantageous to the formation of amorphous mirror-like film as shown in Supplementary Fig. 3. Meanwhile, there might be a competed relationship while the PbI_2/SnI_2 complexes with DMSO. The SnI_2 is supposed to govern the complexing process owing to its higher activation energy. Afterward, the presence of CH_3NH_3I (MAI) will exchange DMSO due to its higher affinity ability toward PbI_2/SnI_2 in comparison to DMSO, which allows the formation of $CH_3NH_3Pb_{(1−x)}Sn_xI_3$ ($0 \leq x \leq 1$) thin films with highly dense and full coverage. As discussed above, the phase of perovskite thin film strongly depends on the x value. When $x < 0.5$, the structure is assigned to be tetragonal phase, whereas it is cubic phase once $x \geq 0.5$ (Fig. 2b).

Figure 3a exhibits the UV-vis absorbance of series $CH_3NH_3Pb_{(1−x)}Sn_xI_3$ ($0 \leq x \leq 1$) thin films. With the Sn content increased, the optical absorbance band-edge of thin film clearly moved toward infrared region in consideration of the narrowed bandgap of $CH_3NH_3SnI_3$. Figure 3b displays the PL spectra of series $CH_3NH_3Pb_{(1−x)}Sn_xI_3$ ($0 \leq x \leq 1$) thin films. In the case of $x = 0$, the PL spectrum was located at 775 nm, which was assigned to the recombination of electron-hole pair for the typical $CH_3NH_3PbI_3$ thin film[24,25]. Again, the intermediate perovskite thin films exhibited an infrared shift with Sn content increasing. The corresponding PL spectrum was consequently fixed at 985 nm. In the case of $x = 1$, i.e. the case of pure $CH_3NH_3SnI_3$ thin film, unexpectedly, the PL spectrum shift to shorter wavelength (955 nm) in comparison to the case of $x = 0.75$. Similar phenomenon was also observed in the previous report[11], which was associated with the tunable bandgap for the intermediate-alloyed compounds of $CH_3NH_3Pb_{(1−x)}Sn_xI_3$ ($0 \leq x \leq 1$).

It was demonstrated that the Sn^{2+} was easily oxidized into Sn^{4+}, which likely cause the instability of Sn-based perovskite solar cells[19]. To study the stability of as-prepared $CH_3NH_3Pb_{(1−x)}Sn_xI_3$ ($0 \leq x \leq 1$) thin films, we carried out its XPS characterizations (Fig. 3c). As expected, we did not detect any signal from the Sn element in the sample $x = 0$. Once the Sn involved, the peak that assigned to Sn element appeared, which was fitted into two main peaks, the corresponding peaks of 485.8 eV and 486.8 eV were associated with the Sn^{2+} and Sn^{4+}, respectively. There was a tendency that the Sn^{2+} decreased, whereas the Sn^{4+} increased while enhancing the Sn content in the perovskite thin films. It appeared that the content of Pb is able to stabilize Sn in its 2+ state somehow. Likewise, the O peaks located at 530.5 eV that were fitted and assigned to SnO_2, which tent to appear and strengthen with the Sn introduction amount increasing (Supplementary Fig. 5). This variation further certified that the $CH_3NH_3Pb_{(1−x)}Sn_xI_3$ ($0 \leq x \leq 1$) thin films preferred to be oxidized while the Pb^{2+} content decreased as we mentioned previously. As expected, the peak intensity of Sn element gradually enhanced, whereas the one of Pb displayed a decreased trend with the Sn introduction amount increasing. Besides, the peak positions of Pb and I elements had a small shift while varying the x value, such fluctuation implies that the coordination environment of Pb and/or I was altered when Sn^{2+} was introduced inside the crystal lattice.
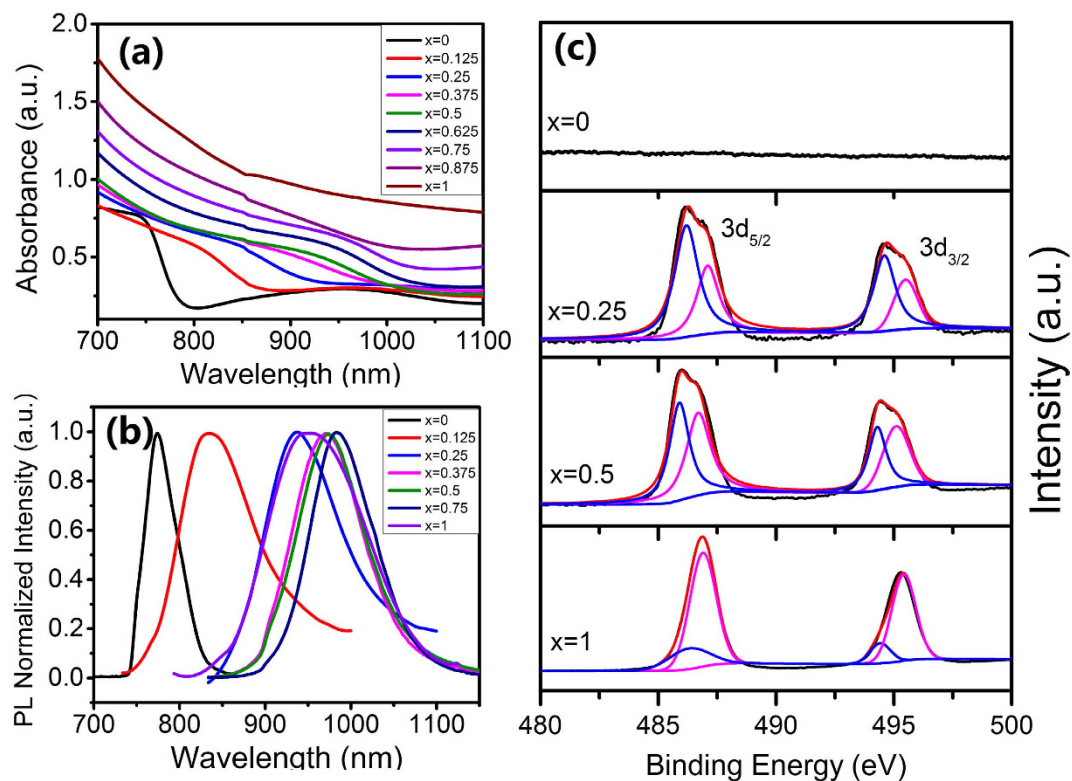
Figure 3. (**a**) UV-vis absorption spectra, (**b**) PL spectra and (**c**) XPS spectra of $Sn3d_{3/2}$ and $Sn3d_{5/2}$ of $CH_3NH_3Pb_{(1-x)}Sn_xI_3$ ($0 \leq x \leq 1$) thin films with different Sn concentrations.

Figure 4 shows the representative SEM images and the corresponding EDS element mapping of Pb, Sn and I in the $CH_3NH_3Pb_{0.75}Sn_{0.25}I_3$ film. Apparently, the Sn, Pb and I were homogeneously distributed throughout the film without any obvious phase separation. We also quantified the atomic ratio of Sn over Sn+Pb as the function of Sn introduction amount by EDS analysis as shown in Fig. 4c. We note that significantly less Sn was presented in the final perovskite than added to the precursor in the intermediary concentrations. The loss of the Sn in the final perovskite films was likely associated with the lower solubility of Sn^{2+} in isopropanol. Particularly, in such two-step process, while the CH_3NH_3I precursor solution in isopropanol was dropped on the SnI_2/PbI_2 film, a little amount of SnI_2 was dissolved and thrown off with the spin coating process. Supplementary Fig. 4 clearly demonstrates the morphology evolution of $CH_3NH_3Pb_{(1-x)}Sn_xI_3$ thin films from x = 0 to x = 1. With the Sn content increasing, the grain sizes of perovskite tent to be enlarged. However, the roughness and coverage of the film suddenly become very poor in the case of x = 1, which further certifies that the presence of lead is able to stabilize the Sn perovskite thin films as mentioned above. Likewise, considering that the growth rate of SnI_2-based complex was faster than that of PbI_2-based complex, the cubic phase of $CH_3NH_3Pb_{(1-x)}Sn_xI_3$ (x ≥ 0.5) thin films were easier to obtain. In such two-step process, we can immediately obtain the cubic Sn-rich perovskite film once spin coating MAI precursor solution at room temperature, which usually gave rise to the film with bigger crystal size but a lower coverage (Supplementary Fig. 4). In this regard, the current two-step procedure was favorable to prepare the Pb-rich and Sn-poor perovskite films. One-step solution-process with the same precursor solution might be more suitable to prepare Pb-free perovskite films.

Photovoltaic performances of $CH_3NH_3Pb_{(1-x)}Sn_xI_3$ ($0 \leq x \leq 1$) perovskite solar cells. Perovskite solar cells with an inverted structure of FTO/PEDOT:PSS/Perovskite/PCBM/BCP/Ag were then fabricated by the series $CH_3NH_3Pb_{(1-x)}Sn_xI_3$ ($0 \leq x \leq 1$) thin films (Supplementary Fig. 6). The use of PEDOT:PSS as hole transport material (HTM) can effectively avoid deteriorating the cells by the commonly used HTM including spiro-OMeTAD, lithiumbis(trifluoromethylsulfonyl) imide salt, and 4-tert-butylpyridine. Figure 5a gives the I–V curves of corresponding cells. The $CH_3NH_3PbI_3$ solar cell shows a decent fill factor (FF) of 80.9%, short-circuit photocurrent density (J_{sc}) of 20.98 mAcm^{-2}, an open-circuit voltage (V_{oc}) of 0.918 V, yielding a PCE of 15.58% under AM1.5G solar illumination. While the Sn species were introduced inside the perovskite thin film, the V_{oc} of corresponding cell decreased, whereas the J_{sc} had a notable enhancement in virtue of the extending absorbed edge. The decreased V_{oc} was ascribed to the lower conduction band edge with decreasing Pb content[26]. After carefully optimized the technic parameters, the maximum PCE of $CH_3NH_3Pb_{0.75}Sn_{0.25}I_3$ perovskite solar cells can rise up to 14.12%, which, to our knowledge, is the highest reported value so far. In the present study, x = 0.25 appears to be the optimum condition by means of banlancing the tradeoff between Pb-content and photovoltaic performances. We then characterized the I–V curves of $CH_3NH_3PbI_3$ and $CH_3NH_3Pb_{0.75}Sn_{0.25}I_3$ by using 55 cells and gave the statistics on photovoltaic results, forward and backward scan as shown in Table 1. The results show
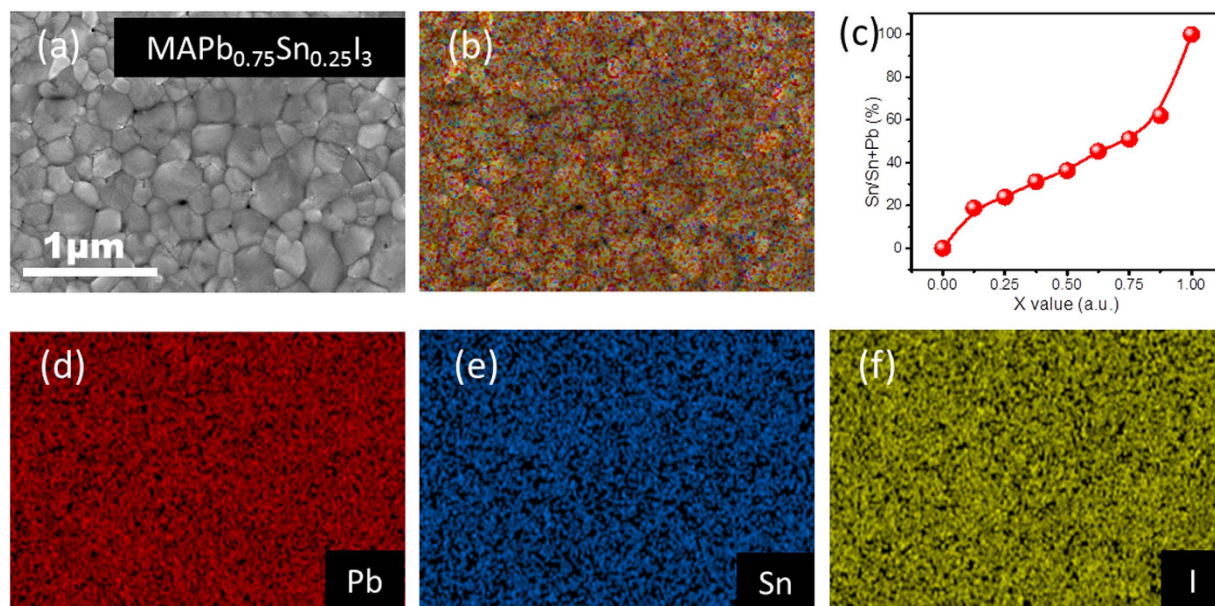
Figure 4. (**a**) Representative SEM images; (**b**,**d**,**e** and **f**) the corresponding EDS elemental mapping of Pb, Sn and I in $CH_3NH_3Pb_{0.75}Sn_{0.25}I_3$, the scale bar is $1\,\mu m$. (**c**) the calculated ratio of Sn:(Sn+Pb) with different Sn introduction amount.
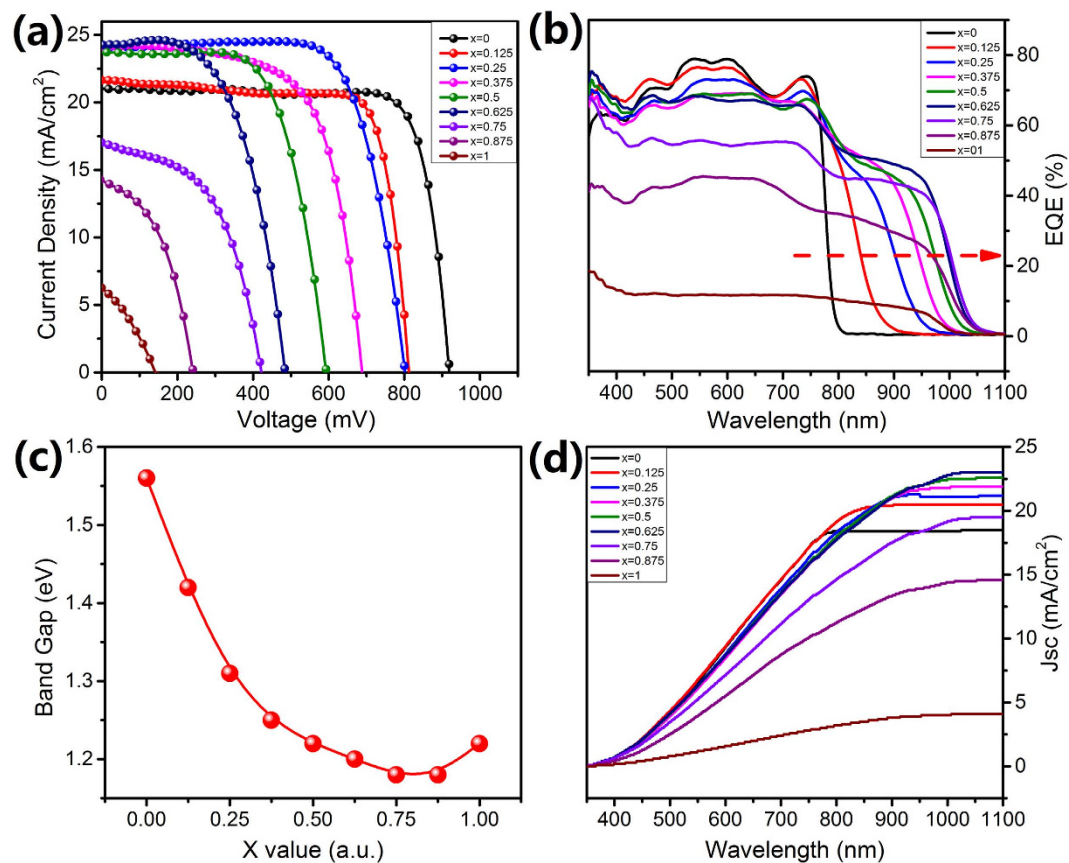
Figure 5. (**a**) I–V curves of $CH_3NH_3Pb_{(1-x)}Sn_xI_3$ ($0 \le x \le 1$) solar cells with different Sn concentrations; (**b**) the corresponding EQE spectra of the cells; (**c**) the calculated bandgap of $CH_3NH_3Pb_{(1-x)}Sn_xI_3$ ($0 \le x \le 1$) thin films with different Sn concentrations; (**d**) the integrated J_{sc} based on the EQE results.

Samples		V_{oc}/mV	J_{sc}/mA·cm^{-2}	FF/%	PCE/%
CH$_3$NH$_3$PbI$_3$ Average	Forward	944 ± 19.3	20.29 ± 1.2	71.11 ± 3.25	13.61 ± 0.68
	Reverse	941 ± 13.5	19.86 ± 1.05	71.02 ± 2.7	13.3 ± 1.07
CH$_3$NH$_3$PbI$_3$ Champion	Forward	957.8	20.65	74.16	14.67
	Reverse	957.8	20.24	73.30	14.21
CH$_3$NH$_3$Pb$_{0.75}$Sn$_{0.25}$I$_3$ Average	Forward	757 ± 22.7	22.82 ± 1.29	70.9 ± 2.6	12.25 ± 0.76
	Reverse	759 ± 21.3	22.35 ± 1.26	74.48 ± 3.1	12.63 ± 0.77
CH$_3$NH$_3$Pb$_{0.75}$Sn$_{0.25}$I$_3$ Champion	Forward	745.4	23.87	74.74	13.3
	Reverse	745.4	23.8	78.56	13.93

Table 1. Statistics of device performance of CH$_3$NH$_3$PbI$_3$ and CH$_3$NH$_3$Pb$_{0.75}$Sn$_{0.25}$I$_3$ cells.

that both CH$_3$NH$_3$PbI$_3$ and CH$_3$NH$_3$Pb$_{0.75}$Sn$_{0.25}$I$_3$ cells have relatively lower hysteresis effects. Likewise, we futher checked the stability under illumination of the CH$_3$NH$_3$PbI$_3$ and CH$_3$NH$_3$Pb$_{0.75}$Sn$_{0.25}$I$_3$ cells, which was shown in Supplementary Fig. 7. In comparision to pure Pb-based device, more or less Sn-involved inside the perovskite thin films would lead to inferior stability of the corresponding cells, which was consistent with the previous report[18]. The oxidation of Sn^{2+} in air might be the main cause that quenched the photovoltaic poerformances of the Sn-based solar cells. Careful encapsulation technology is under study and would resolve the instability of Sn-based solar cell. It is worthy of noting that the PCE of cells with different amount of Sn species here overall outperformed the ones with same Sn content in previous report[11]. As shown in Fig. 5b, the external quantum efficiency (EQE) of series CH$_3$NH$_3$Pb$_{(1-x)}$Sn$_x$I$_3$ ($0 \leq x \leq 1$) solar cells were demonstrated to cover the whole visible spectrum and realize a broad absorption minimum over 50% from 350 to 950 nm accompanied by a noteworthy absorption onset up to 1050 nm. It should be mentioned that the CH$_3$NH$_3$SnI$_3$ solar cell had an ultraviolet-shift in comparison to the case of CH$_3$NH$_3$Pb$_{0.25}$Sn$_{0.75}$I$_3$, which was consistent with the PL characterizations. We calculated the band gap of CH$_3$NH$_3$Pb$_{(1-x)}$Sn$_x$I$_3$ ($0 \leq x \leq 1$) thin films based on the EQE (Fig. 5c). It clearly pointed out that we can easily tune the bandgap of perovskite thin film between 1.18 and 1.56 eV. The intermediate compounds with $x = 0.75$ exhibited the smallest bandgap of 1.18 eV. Meanwhile, we integrated the J$_{sc}$ that estimated from EQE (Fig. 5d), which were in consistent with the measured J$_{sc}$ as shown in Fig. 5a.

Discussion

The pure Sn-based perovskite thin film still suffered from the poor perovskite film quality and low coverage, which gave rise to a poor photovoltaic performance. In the present system, we assumed that the pure SnI$_2$ was not able to effectively complex the DMSO to form the intermediate compound in view of its higher activation energy toward crystallization, thus enabling the SnI$_2$ to crystallize quickly just as the case without any solvent mediation. Moreover, the presence of Sn^{4+} in CH$_3$NH$_3$SnI$_3$ thin film might also contribute to the quenched J$_{sc}$. More studies on the stability of CH$_3$NH$_3$SnI$_3$ solar cells, e.g. solvent engineering, professional encapsulation are underway.

In summary, we employed DMSO to intercalate inside the lattice structure of PbI$_2$/SnI$_2$, which allowed the formation of intermediate complexes of PbI$_2$/(SnI$_2$)·(DMSO)$_x$, by which, the CH$_3$NH$_3$Pb$_{(1-x)}$Sn$_x$I$_3$ ($0 \leq x \leq 1$) thin films with full coverage and decent grain size can be obtained. The tunable bandgap and high quality of Sn-introduced perovskite thin films facilitated the realization of solar cells with maximum PCE of 14.12%. We believe that our study can shed lights on the realization of highly efficient Pb-free perovskite solar cells.

Methods

Film preparation and device fabrication. The fluorine doped tin oxide (FTO)-coated glass (8 Ω/cm^2, Nippon) was cleaned with deionized water, acetone and alcohol in an ultrasonic washing unit by turn. After dried under N$_2$ atmosphere, the glass was treated under oxygen plasma for 10 min. PEDOT:PSS (Heraeus-Clevios P 4083, Xi'an p-OLED) was spun on the as-treated substrate at a speed of 3,500 rounds per minute (r.p.m.). The film was then annealed at 140 °C for 10 min. 170 mg of PbI$_2$ (Alfa Aesar, 99.9985%) and 138 mg SnI$_2$ (Aldrich, 99.99%) were dissolved in the mixed solvent containing 200 μL of DMF (Aldrich, 99.9%) and 40 μL of DMSO (Aldrich, 99.9%), respectively. After heated at 60 °C for 2 h, a certain amount of prepared PbI$_2$ and SnI$_2$ solutions were mixed to form the precursor solution. It's worthy of noting that the PbI$_2$ solution needed to be filtered prior to mixing. The mixed precursor solution was spun on the PEDOT:PSS layer at 5000 (r.p.m.) for 30 s. After natural evaporation for 10 min to form the PbI$_2$(SnI$_2$)·(DMSO)$_x$ complexes, the MAI solution with the concentration of 60 mg/ml was spun on the substrate at 4000 (r.p.m.) for 30 s. Afterward, the obtained thin films were annealed at 120 °C for 20 min. Exceptionally, the pure PbI$_2$-based perovskite film was annealed at 140 °C for 20 min. The [6,6]-phenyl-C61-butyric acid methyl ester (PCBM) dissolved into dichlorobenzene with the concentration of 20 mg/ml was spun on the top of the as-prepared perovskite layers at 2000 (r.p.m.) for 30 s. Finally, 6 nm 2,9-dimethyl-4,7-diphenyl-1,10-Phenanthroline (BCP) and 120 nm Ag electrode were sequentially deposited by thermal evaporation. Note that all of the film fabrications were processed in nitrogen-filled glovebox.

Characterizations. The crystal structure was characterized by Bruker D8 Advance X-ray diffractometer (XRD) with CuKα radiation at 40 kV and 40 mA. Field-emission scanning electron microscopy (SEM) was used to characterize the morphology of the obtained thin film. Both top-down and cross-sectional views were obtained using a FEI NovaNanoSEM450. A double beam spectrophotometer (U-4100, Hitachi) equipped with an integrated sphere was used for the UV-vis transmission measurements in the range from 700 to 1100 nm. A Fourier transform infrared spectroscopy was used to collect the FT-IR spectral data in the 4000 cm^{-1}–400 cm^{-1} range.

The KBr pellet was used for the powdered samples of layer materials scraped from the substrate. X-ray photo-electron spectroscopy (XPS) was measured with a PHI 5300 ESCA Perkin-Elmer spectrometer. All spectra were shifted to account for sample charging using inorganic carbon at 284.80 eV as a reference. The photoluminescence (PL) was carried out under the excitation of a 532-nm continuous-wave laser. The PL signal is sent to a 0.5-m spectrometer through a $50\times$ objective lens and then detected by a liquid nitrogen-cooled CCD detector array. All PL spectrums were normalized.

Current-voltage (J-V) characteristics of perovskite solar cells were measured using a semiconductor device analyzer (Keithley 2601B) and a SAN-EI solar simulator (XES-100S1) with an AM 1.5 G spectrum. The illumination power on the sample was adjusted to $1000\,W\,m^{-2}$ using a certified reference solar cell (RS-ID-4). A black mask with an aperture ($9\,mm^2$) was placed on the top of the device to control the effective electrode area. Both forward and backward scans were performed and the scan speed was fixed at 0.15 V/s. The external quantum efficiency (EQE) of perovskite solar cell device was measured by using spectrum corresponding system (QTesT 1000ADX), with the monochromatic light wavelength ranging from 350 nm to 1100 nm. The monochromatic light beam is produced by a dual grating monochromatic in front of a halogen lamp. A Si reference solar cell with known EQE is used to determine the spectral response of perovskite solar cells.

References

1. Kojima, A., Teshima, K., Shirai, Y. & Miyasaka, T. Organometal halide perovskites as visible-light sensitizers for photovoltaic cells. *J. Am. Chem. Soc.* **131,** 6050–6051 (2009).
2. Im, J. H., Lee, C. R., Lee, J. W., Park, S. W. & Park, N. G. 6.5% efficient perovskite quantum-dot-sensitized solar cell. *Nanoscale* **3,** 4088–4093 (2011).
3. Burschka, J. *et al.* Sequential deposition as a route to high-performance perovskite-sensitized solar cells. *Nature* **499,** 316–319 (2013).
4. Liu, M., Johnston, M. B. & Snaith, H. J. Efficient planar heterojunction perovskite solar cells by vapour deposition. *Nature* **501,** 395–398 (2013).
5. Zhou, H. *et al.* Interface engineering of highly efficient perovskite solar cells. *Science* **345,** 542–546 (2014).
6. Yang, W.-S. *et al.* High-performance photovoltaic perovskite layers fabricated through intramolecular exchange. *Science* **348,** 1234–1237 (2015).
7. Bi, D. *et al.* Efficient luminescent solar cells based on tailored mixed-cation perovskites. *Sci. Adv.* **2,** e1501170, 10.1126/sciadv.1501170 (2016).
8. Green, M. A., Ho-Baillie, A. & Snaith, H. J. The emergence of perovskite solar cells. *Nat. Photon.* **8,** 506–514 (2014).
9. Hodes, G. & Cahen, D. Perovskite cells roll forward. *Nat. Photon.* **8,** 87–88 (2014).
10. Niu, G. *et al.* Study on stability of $CH_3NH_3PbI_3$ films and effect of post modification by Aluminum oxide in all-solid-state hybrid solar cells. *J. Mater. Chem. A* **2,** 705–710 (2014).
11. Hao, F., Stoumpos, C. C., Chang, R. P. & Kanatzidis, M. G. Anomalous band gap behavior in mixed Sn and Pb perovskites enables broadening of absorption spectrum in solar cells. *J. Am. Chem. Soc.* **136,** 8094–8099 (2014).
12. Ogomi, Y. *et al.* $CH_3NH_3Sn_xPb_{(1-x)}I_3$ Perovskite solar cells covering up to 1060 nm. *J. Phys. Chem. Lett.* **5,** 1004–1011 (2014).
13. Zuo, F. *et al.* Binary-metal perovskites toward high-performance planar-heterojunction hybrid solar cells. *Adv. Mater.* **26,** 6454–6460 (2014).
14. Babayigit, A., Ethirajan, A., Muller, M. & Conings, B. Toxicity of organometal halide perovskite solar cells. *Nat. mater.* **15,** 247–251 (2016).
15. Babayigit, A. *et al.* Assessing the toxicity of Pb-and Sn-based perovskite solar cells in model organism Danio rerio. *Sci. Rep.* **6,** 18721, 10.1038/srep18721 (2016).
16. Hao, F., Stoumpos, C. C., Cao, D. H., Chang, R. P. H. & Kanatzidis, M. G. Lead-free solid-state organic–inorganic halide perovskite solar cells. *Nat. Photon.* **8,** 489–494 (2014).
17. Noel, N. K. *et al.* Lead-free organic-inorganic tin halide perovskites for photovoltaic applications. *Energy Environ. Sci.* **7,** 3061–3068 (2014).
18. Hao, F. *et al.* Solvent-mediated crystallization of $CH_3NH_3SnI_3$ films for heterojunction depleted perovskite solar cells. *J. Am. Chem. Soc.* **137,** 11445–11452 (2015).
19. Lee, S. J. *et al.* Fabrication of efficient formamidinium tin iodide perovskite solar cells through SnF_2-pyrazine complex. *J. Am. Chem. Soc.* **138,** 3974–3977 (2016).
20. Li, W., Fan, J., Li, J., Mai, Y. & Wang, L. Controllable grain morphology of perovskite absorber film by molecular self-assembly toward efficient solar cell exceeding 17%. *J. Am. Chem. Soc.* **137,** 10399–10405 (2015).
21. Chen, Q. *et al.* Controllable self-induced passivation of hybrid lead iodide perovskites toward high performance solar cells. *Nano lett.* **14,** 4158–4163 (2014).
22. Kim, Y. C. *et al.* Beneficial effects of PbI_2 incorporated in organo-lead halide perovskite solar cells. *Adv. Energy Mater* **6,** 1502104, 10.1002/aenm.201502104 (2016).
23. Liu, C. *et al.* Hysteretic behavior upon light soaking in perovskite solar cells prepared via modified vapor-assisted solution process. *ACS Appl. Mater. Interfaces* **7,** 9066–9071 (2015).
24. Stranks, S. D. *et al.* Electron-hole diffusion lengths exceeding 1 micrometer in an organometal trihalide perovskite absorber. *Science* **342,** 341–344 (2013).
25. Xing, G. *et al.* Long-range balanced electron- and hole-transport lengths in organic-inorganic $CH_3NH_3PbI_3$. *Science* **342,** 344–347 (2013).
26. Kim, H. S. *et al.* Mechanism of carrier accumulation in perovskite thin-absorber solar cells. *Nat. commun.* **4,** 2242, 10.1038/ncomms3242 (2013).

Acknowledgements

Author Contributions

Additional Information

Supplementary information accompanies this paper at http://www.nature.com/srep

Competing financial interests: The authors declare no competing financial interests.

How to cite this article: Liu, C. *et al.* Highly Efficient Perovskite Solar Cells with Substantial Reduction of Lead Content. *Sci. Rep.* **6**, 35705; doi: 10.1038/srep35705 (2016).